Materials Science-Poland, *Vol. 28*, *No. 2*, *2010*

Humidity sensing properties of TiO_2–Sb_2O_5 nanocomposite

A. K. SRIVASTAVA, B. C. YADAV*

Nanomaterials and Sensors Research Laboratory, Department of Physics,
University of Lucknow, Lucknow-226007, India

The syntheses of TiO_2–Sb_2O_5 (AT) composites were investigated by the conventional precipitation method and their use as humidity sensors. 2–50 wt. % of Sb_2O_5 was added to TiO_2 and pellets were made under the pressure of 616 MPa a room temperature of 30ºC. The pellets were annealed at various temperatures (200, 500, 700 and 800 °C) for 3 h and the humidity sensing properties of each pellet were studied. A saturated aqueous solution of potassium sulphate was used as the humidifier and a saturated solution of potassium hydroxide was used as the dehumidifier. Upon increasing relative humidity (*RH*) inside the test chamber, the resistance of each pellet decreased for the *RH* range from 10% to 95%. Samples of the sensor material, differing in the percentage of the additive, were subject to SEM and XRD analysis. The minimum grain size, estimated from SEM, was 30 nm and the minimum crystallite size from XRD data was 20 nm. The material was found to have suitable properties to be applied as a resistive humidity sensor operating over the entire humidity range.

Keywords: *titania; humidity; nanocomposite; resistance; sensor; adsorption*

1. Introduction

TiO_2 is an important technological material used in electronic [1], electrical [2, 3], optical [4–6] and catalytic devices [7, 8] due to of its high electric permittivity, large birefringence, chemical stability and high photocatalytic activity. Physical properties of TiO_2 have been the subject of various investigations in terms of its suitability for various applications. TiO_2 occurs in three crystalline polymorphs: rutile, anatase and brookite, rutile being the most stable phase. Doping with impurities such as In, Cr, Cd, Fe and Co can change the magnetic and semiconducting properties of TiO_2. Among various oxide semiconductors, titania appears promising and important for the use in environmental purification, due to its strong oxidizing power, non-toxicity and long

*Corresponding author; e-mail: balchandra_yadav@rediffmail.com

term photostability. Many authors studied the synthesis, structure, and humidity sensitive electrical conduction of material containing TiO_2 [7–18].

We have already reported on the humidity sensing properties of pure TiO_2, but reproducibility was poor and the ageing effect was 91% during six months of observations. Therefore in order to improve the quality and sensing characteristics of humidity sensor, TiO_2–Sb_2O_5 (AT) composite has been investigated as the sensing material, fabricated by the conventional precipitation method. Sb_2O_5 was mixed with TiO_2 in various proportions and the dependence of the resistance on the humidity was measured.

2. Operating principles of the sensor

Ceramic humidity sensors exhibit chemical resistance [19]. The conductivity of such sensing materials depends on the amount of adsorbed water vapour. This principle is employed for the measurement of humidity in resistive type humidity sensors. This type of sensors can be subdivided into ionic-type and electronic-type humidity ones, depending on their conduction mechanism. The sensing mechanism generally accepted for porous oxides at room temperature is of the ionic type. Morimoto et al. [20] established that the changes in impedance of porous ceramics dependent on environmental humidity are related to the mechanism of water adsorption on the oxide surface. At low humidities, conduction is due to proton hopping between hydroxyl ions on the first layer of chemisorbed water, while at higher humidities, protons hop between physisorbed molecules according to the Grotthuss chain reaction mechanism. The morphology of the sensing element influences water vapour adsorption and desorption. The condensation of water vapour occurs as a result of capillary action. The behaviour of this condensation is a function of ceramic pore size and their distribution.

The sensitivity S of a humidity sensor has been defined as a change in resistance ΔR of a sensing element per unit change in relative humidity RH

$$S = \frac{\Delta R}{\Delta RH}$$

The porosity P of the material was determined from its density, according to the following expression:

$$P = \frac{\rho_{th} - \rho_m}{\rho_{th}} \times 100\%$$

where ρ_{th} ρ_m are the theoretical and measured densities, respectively. The theoretical densities of anatase and rutile TiO_2 are 3.84 and 4.24 g·cm^{-3}, respectively. Since the specimen is a circular pellet, the density was determined by measuring its volume and weight.

3. Experimental

Preparation of the sensing element. For fabrication of the sensing element, $SbCl_3$ was mixed with deionized water and stirred for 3 h. The precipitate was filtered and washed several times with deionized water in order to remove chloride ions. After drying, the powder was added to titania in the proportion 2, 5, 10, 20, 30, 40 and 50 wt. %. On vigorous grinding of the material, using a mortar and pestle, for 6 h, a very fine powder was produced. Pellets of this material were then subject to the pressure of 616 MPa at room temperature, using a hydraulic pressing machine. Each pellet was 9 mm in diameter, 5 mm thick. The pellets were annealed at various temperatures (200, 500, 700 and 800 °C) for 3 h inside an electric furnace. Each pellet was secured in an electrode holder and was exposed to various humidities in a humidity chamber. Resistances in function of humidity were measured using a digital multimeter (VC 9808, India). Relative humidity was measured using a standard hygrometer (Huger, Germany). The minimum hygrometer reading in our tests was $RH = 1$ %.

Surface morphology and crystal structure. Surface morphology was studied using a scanning electron microscope (SEM, LEO-0430, Cambridge). The micrographs shown in Figs. 1–5 reveal that molecules of TiO_2–Sb_2O_5 are agglomerated, of uniform size, equally distributed and highly porous, having the grain size of 30–120 nm and the average pore size of 80 nm. Higher porosity increases the surface-to-volume ratio of the material and, therefore, improves the sensitivity of the sensor material. Figure 1 shows SEM of 2% AT nanocomposite: clusters with small pores can be seen. In the SEM of 5% AT nanocomposite (Fig. 2) clusters with improved pores were identified. Figures 3 and 4 show SEM of 10% AT and 30% AT nanocomposites, respectively. Grains are less agglomerated and pore sizes increase. In the SEM of 50% AT nanocomposite (fig. 5), uniform flower-like morphology can be seen. Pores are largest in this photograph.

X-ray diffraction data, obtained with an X-Pert PRO XRD system (Netherland), having a CuK_α radiation source with the wavelength of 1.54 Å, shows the extent of crystallization of the TiO_2–Sb_2O_5 sensing element, annealed at 700 °C; the pattern is shown in Fig. 6. It reveals that the sensing material consists of titania and antimony oxide. Analysis shows that TiO_2 exists in an excess amount. Its peaks occur at 2θ values of 25.3, 37.0, 37.8, 38.6, 48.0, 53.9, 55.1, 62.2, 62.8, 70.4 and 74.1°. These peaks have d values of 3.513, 2.429, 2.378, 2.330, 1.890, 1.699, 1.664, 1.492, 1.480, 1.336 and 1.279 Å, with corresponding planes (101), (103), (004), (112), (200), (105), (211), (213), (204), (220) and (107), respectively. Peaks for Sb_2O_5 exist at 2θ values of 15.0, 24.6, 29.0, 30.3, 35.1, 46.1, 50.5, 53.0, 60.0 and 68.7°, with corresponding planes (111), (220), (311), (222), (400), (511), (440), (531), (622) and (642). The d values for these peaks are found to be 5.900, 3.613, 3.081, 2.950, 2.555, 1.967, 1.807, 1.728, 1.540 and 1.366 Å, respectively. Using the well known

Debye–Scherrer formula, the crystallite size was calculated (Table 1). The minimum size of the crystallite was found to be 20 nm, corresponding to the (531) plane, and maximum size was 112 nm, corresponding to the (112) plane.

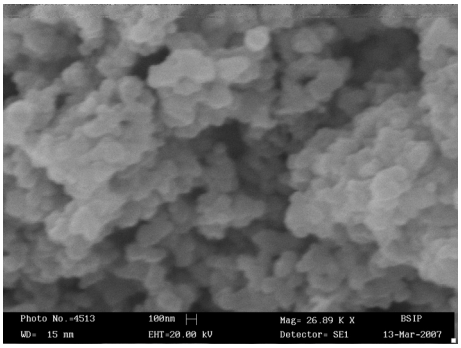

Fig. 1. Scanning electron micrograph of 2% AT nanocomposite

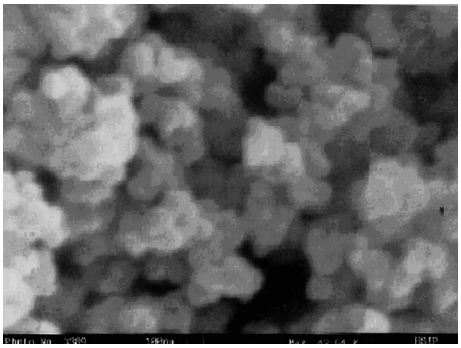

Fig. 2. Scanning electron micrograph of 5% AT nanocomposite

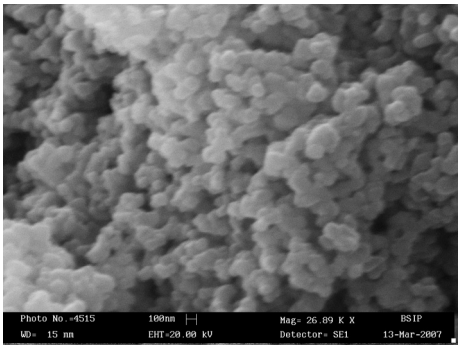

Fig. 3. Scanning electron micrograph of 10% AT nanocomposite

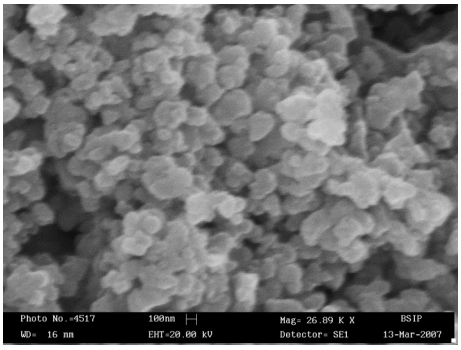

Fig. 4. Scanning electron micrograph of 30% AT nanocomposite

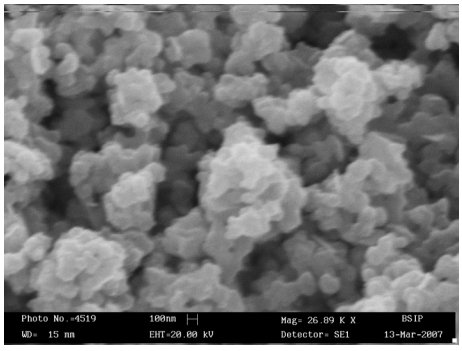

Fig. 5. Scanning electron micrograph of 50% AT nanocomposite

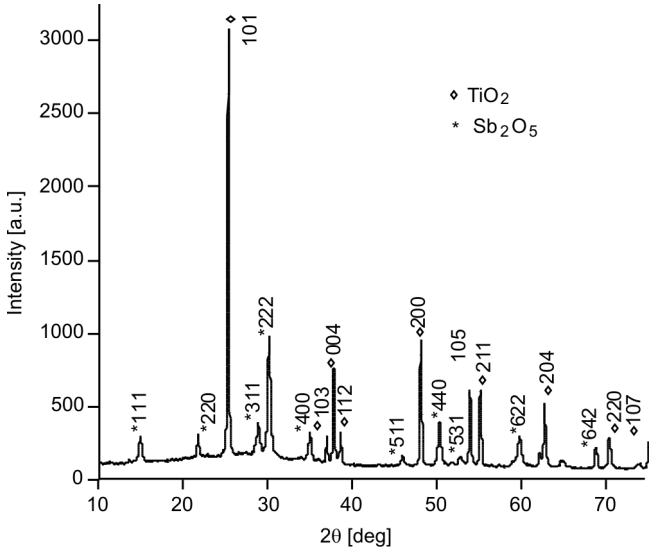

Fig. 6. X-ray diffraction pattern of 50% AT nanocomposite annealed at 700 °C

Table 1. Particles sizes calculated for various peaks with corresponding 2θ and FWHM values for 50% AT annealed at 700 °C

2θ [deg]	FWHM (β)	D [nm]
15.0	0.2204	38
24.6	0.0945	88
25.0	0.0945	90
29.0	0.1574	55
30.3	0.1417	61
35.1	0.2204	40
37.0	0.0787	111
37.8	0.0945	93
38.6	0.0787	112
46.1	0.3149	29
48.0	0.1152	79
50.5	0.2304	40
53.0	0.4608	20
54.0	0.1344	69
55.0	0.1152	81
60.0	0.3072	31
62.2	0.1152	84
62.8	0.1536	63
68.7	0.1920	52
70.4	0.1536	66

Device assembly. The device assembly is shown in Fig. 7a, and a schematic diagram of the pellet holder is shown in Figure 7b. The Cu–pellet–Cu electrode arrange-

ment is fixed on a non-conducting base inside the chamber such that the connecting wires remain outside the chamber. A saturated aqueous solution of potassium sulphate, increasing the humidity, is placed in a small container inside the steel chamber.

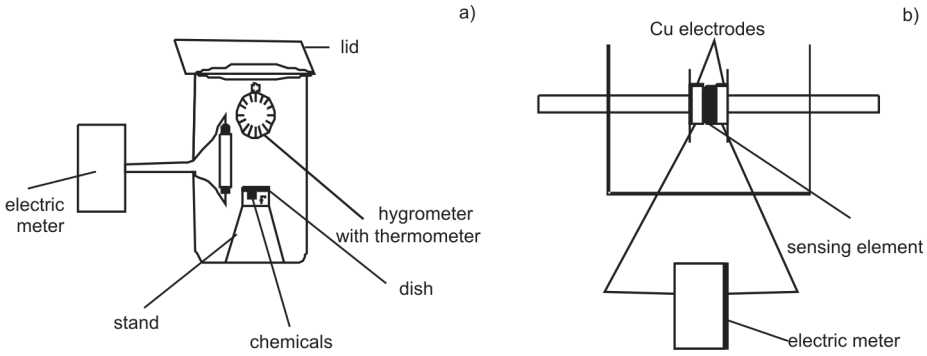

Fig. 7. Schematic diagrams of the device assembly (a) and of the Pellet holder (b)

The percentage relative humidity (*RH*) inside the chamber is increased from 10% to 95%. The resistance of TiO_2–Sb_2O_5 pellets in function of *RH* was recorded. The chamber was then dehumidified up to *RH* = 10%, by placing inside a dish of saturated salt solution of potassium hydroxide in deionized water. *RH* was measured with a standard hygrometer (Huger, Germany). A thermometer with the accuracy of ±1°C was hung in the chamber. Variations in the resistance were recorded using a sinometer of MΩ order (VC 9808).

4. Results and discussion

In Figure 8a, the dependences of the resistance on the relative humidity are shown for sensing elements of AT (2%, 5%, 10% and 20%) after annealing at 200 °C for 3 h. The curve for 2% AT shows that as the *RH* increases up to 25%, the resistance decreases drastically, whereas further increases in the *RH* yields a more gradual decrease in resistance, up to the point of saturation. The data for 5% AT shows that as the *RH* increases up to 30%, the resistance decreases rapidly, and then upon further increase in the *RH*, it decreases gradually up to *RH* of 95%. Data curves for 10% AT show that as *RH* increases up to 35%, the resistance decreases drastically and then it decreases gradually, up to the point of saturation. The data curve for 20% AT exhibits a similar profile to that for 5% AT, except that it has higher resistance at low humidity. Figure 8b shows the variation of resistance with respect to relative humidity for sensing elements of AT (30%, 40% and 50%) prepared under the same conditions as above. The data for 30% AT shows that as the *RH* increases up to 40%, the resistance decreases sharply, and then further increases, the *RH* yields a gradual decrease in the resistance up to the point of saturation. The data for 40% AT shows that as the *RH*

increases up to 45%, the resistance decreases rapidly, and then further increases in *RH* cause it to decrease gradually, up to an *RH* of 95%. Data for 50% AT shows that as the *RH* increases up to 55%, the resistance decreases drastically, and then it decreases gradually up to the point of saturation.

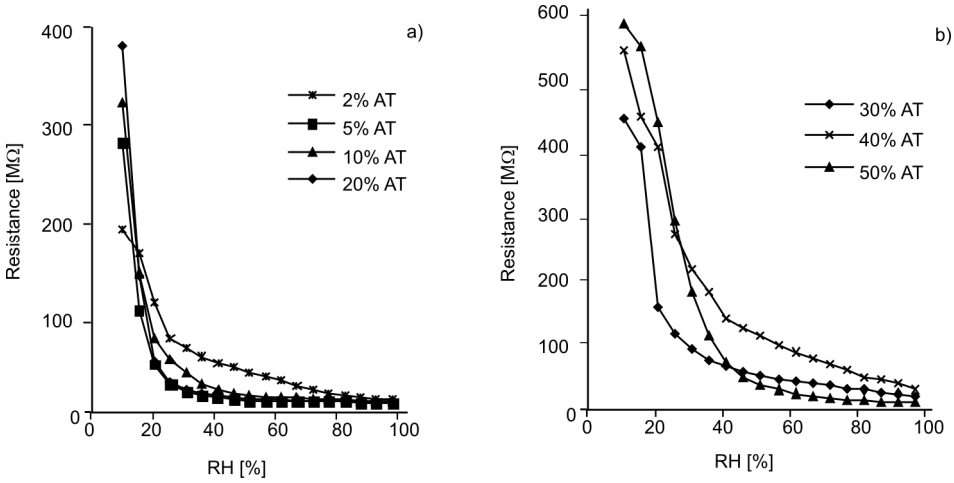

Fig. 8. Dependences of resistances of AT nanocomposites on the *RH* of sensing element of: a) 2%, 5%, 10% and 20%, b) 30%, 40% and 50%, all annealed at 200 °C

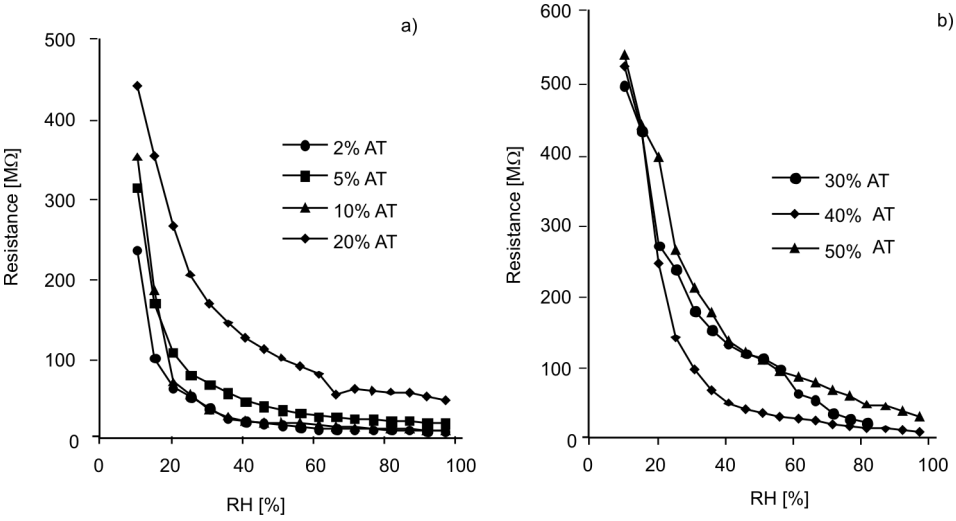

Fig. 9. Dependences of resistances of AT nanocomposites on the *RH* of sensing element of: a) 2%, 5%, 10% and 20%, b) 30%, 40% and 50%, all annealed at 500 °C

Figure 9a shows the dependences of the resistance on the relative humidity for AT sensing elements (2%, 5%, 10% and 20%) fabricated after annealing at 500 °C for 3 h. The data for 2% AT shows that as the *RH* increases, the resistance decreases drasti-

cally up to *RH* = 20%, and then it decreases gradually to the point of saturation. The data for 5% AT shows that as the *RH* increases up to 25%, the resistance decreases drastically, and then upon further increase in the *RH*, it decreases gradually over the rest of the *RH* range. The data for 10% AT exhibits a similar profile to that of 2% AT. The data for 20% AT shows that as the *RH* increases up to 65%, there is a rapid decrease in the resistance, and for higher *RH* values it decreases gradually up to an *RH* of 95%. Figure 9b shows the dependences of the resistance on the relative humidity for sensing elements of AT (30%, 40% and 50%) fabricated after annealing at 500 °C for 3 h. The data for 30% AT shows that as the *RH* increases up to 70%, the resistance decreases drastically and then, upon further increases in the *RH*, it corresponds to a gradual decrease in the resistance, up to the point of saturation. The data for 40% AT shows that as the *RH* increases up to 70%, the resistance decreases rapidly and, upon further increase in the *RH*, it decreases gradually, up to the *RH* of 95%. The data for 50% AT shows very similar behaviour demonstrating that the material is suitable for designing a sensor.

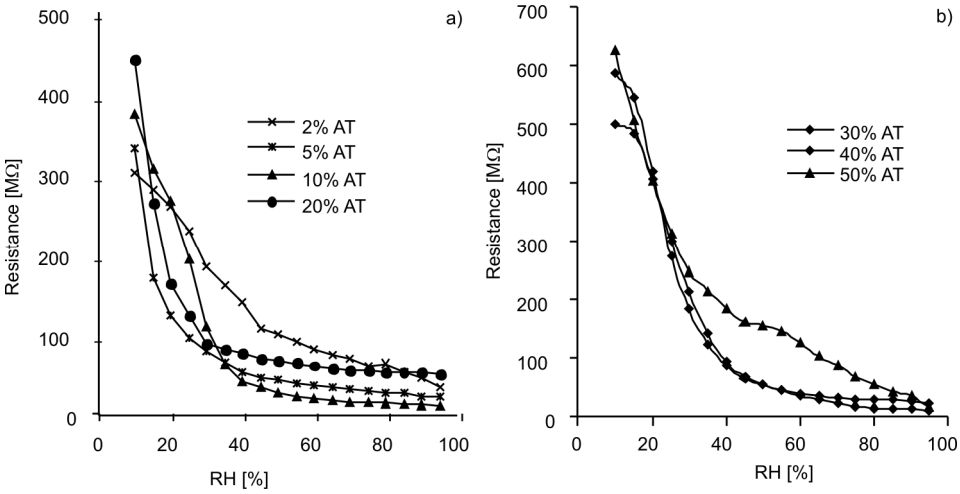

Fig. 10. Dependences of resistances of AT nanocomposites on the *RH* of sensing element of: a) 2%, 5%, 10% and 20%, b) 30%, 40% and 50%, all annealed at 700 °C

Figure 10 shows the dependences of electrical resistance on *RH* for 2%, 5%, 10%, 20% and 30%, 40%, 50% AT. The data for 2% AT (Fig. 10a), shows that as *RH* increases up to 65%, the resistance first decreases drastically, and further increase in *RH* leads to gradual decrease in the resistance up to the point of saturation. Curve for 5% AT shows that as the *RH* increases up to 30%, the resistance decreases rapidly and then, upon further increase in the *RH*, it decreases gradually up to an *RH* of 95%. Data for 10% and 20% AT give similar profile to that corresponding to 5% AT. Figure 10b shows the dependences of the resistance on the relative humidity for sensing elements of AT (30%, 40% and 50%). The data for 30% AT shows that as the *RH* increases up

to 40%, the resistance decreases drastically, and then, upon increasing the *RH*, it yields a gradual decrease in the resistance, up to an *RH* of 95%. The data for 40% AT exhibits a similar profile to that corresponding to 30% AT. The data for 50% AT shows that as the *RH* increases up to 80%, the resistance decreases linearly everywhere in the specified humidity range.

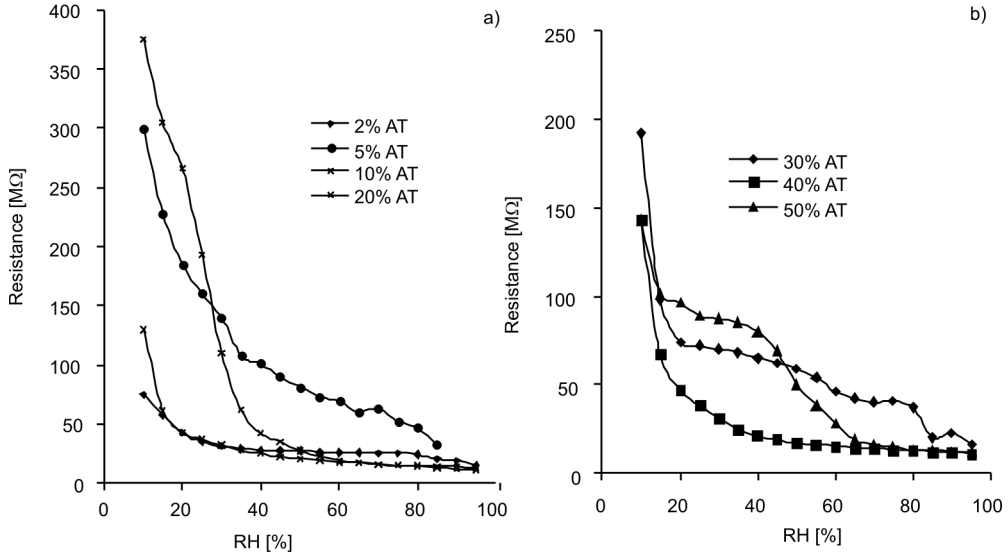

Fig. 11. Dependences of resistances of AT nanocomposites on the *RH* of sensing element of: a) 2%, 5%, 10% and 20%, b) 30%, 40% and 50%, all annealed at 800 °C

Figure 11a shows the dependence of the resistance on the relative humidity, for AT sensing elements prepared by adding 2%, 5%, 10% and 20% wt. % of antimony. The data for 2% AT shows a gradual change in the resistance, up to the point of saturation. The data for the 5% AT sensing element has a better slope, and there is a drastic decrease in the resistance, up to an *RH* of 45%; this decrease was observed to become more gradual, indeed it has a linear response, for higher *RH* values of up to 95%. The data for 10% and 20% AT exhibit a similar profile to that corresponding to 5% AT. Figure 11b shows the variation in the resistance with respect to relative humidity for the sensing elements of AT (30%, 40% and 50%) annealed at 800 °C. The data for 30% AT shows that as the *RH* increases up to 20%, the resistance decreases rapidly and then, upon further increase in the *RH*, it decreases gradually, up to the *RH* of 95%. The data for 40% AT shows that as the *RH* increases up to 15%, the resistance decreases drastically, and then, upon further increase in the *RH*, there is a gradual decrease in the resistance, up to the point of saturation. The data for 50% AT shows that as *RH* increases up to 40%, the resistance decreases rapidly and then, upon further increase in the *RH*, it decreases gradually, for the *RH* of up to 95%.

Figure 12 shows the dependences of the average sensitivity of the composite material annealed at 200, 500, 700 and 800 °C on the contents of Sb_2O_5. For annealing temperatures of 200, 500 and 700 °C, the average sensitivity increases as the percentage of Sb_2O_5 increases. The composite of 50% Sb_2O_5 with TiO_2 exhibits the highest average sensitivity, i.e. 7.5. The sensitivity of the sensing element annealed at 800 °C increases for the additive content up to 5%; for higher contents of the additive, the sensitivity decreases markedly. The sensing material probably becomes amorphous after annealing at 800 °C.

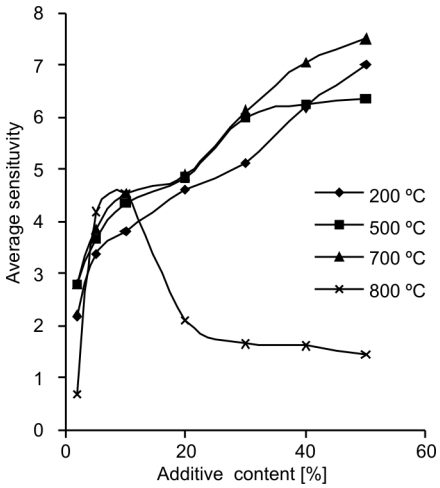

Fig. 12. Dependence of average sensitivity on additive content for the sensing elements annealed at various temperatures

As reported by the Moon et al. [8], the conduction behaviour of TiO_2–Sb_2O_5 in the presence of water vapour mainly depends on the presence of ions. The present study also proves that the conduction in TiO_2–Sb_2O_5 depends on ions, probably protons. In this sensing material, Sb^{3+} cations are assumed to be an highly active sites for adsorption, due to their highest charge density. These ions readily combine with the hydroxyl group of adsorbed water, thereby weakening the bonds between hydroxyl ions and protons: water molecule subsequently becomes dissociated. This provides free protons for electrical conduction. The hydroxyl ions thus remain chemically adsorbed at the cationic sites. Therefore, the first layer of adsorbed water molecule forms a chemisorbed layer, and this process is irreversible at room temperature. The subsequent layers are physically adsorbed on the first layer to form hydroxyl multilayers by hydrogen bonding. These free mobile protons, obtained from the first chemisorbed layer, react with physisorbed water layer and form hydronium ions.

When the physically adsorbed layer is abundant, the protons from one hydronium ion can hop to another hydronium ion; this proton transfer mechanism provides the means by which electrical conduction can occur. The physisorption of the water layer is reversible at room temperature and it exists in equilibrium in ambient humidity conditions. As the ambient humidity varies, the amount of water vapour physisorbed on the surface or condensed on the capillary pores also varies, subsequently changing the

concentration of the mobile protons, which in turn changes the conductivity of the ceramic.

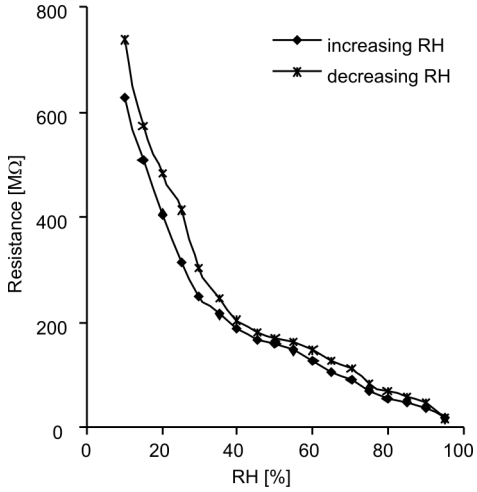

Fig. 13. Hysteresis curve for the sensing element 50% AT annealed at 700 °C

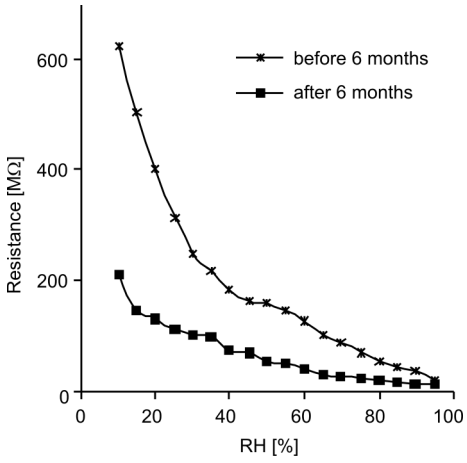

Fig. 14. Dependence of resistance of 50% AT nanocomposite annealed at 700°C on the *RH* of sensing element just after fabrication and after 6 months

The hysteresis curve for the TiO_2–Sb_2O_5 sensing element annealed at 700 °C in Fig. 13 shows 17.61% hysteresis. After humidity treatment, all the sensing elements were kept in a laboratory environment and their humidity sensing characteristics were regularly monitored. Figure 14 shows the dependences of the resistance of the TiO_2–Sb_2O_5 sensing element on the *RH*, both before annealing and 6 months after annealing at 700 °C. It was found that the sensor had become less sensitive to humidity and deteriorated by 67%.

5. Conclusion

TiO_2–Sb_2O_5 nanocomposite was investigated for its humidity sensing characteristics. The nanocrystals in the sensing material annealed at 700 °C had an average size of 20–112 nm, which meant that the material was highly sensitive to the presence of water vapour. Among the samples tested, this sensing element had the highest average sensitivity, namely a maximum sensitivity index of 7.5. Nearly all the sensing elements exhibited a similar profile, i.e. at the minimum *RH* their resistances were reached the maximum values and at the maximum *RH* their resistance were at the minimum. The humidity sensor reported in this paper is cheap and easy to fabricate, user-friendly and is sensitive to the entire *RH* range. This can be exploited in commercial production.

References

[1] FUYUKI T., MATSUNAMI H., Jpn. J. Appl. Phys., 25 (1986), 1288.
[2] YADAV B.C., SRIVASTAVA A.K., SHARMA P., Sen. Trans. J., 81 (2007), 1348.
[3] YADAV B.C., SHARMA P., SRIVASTAVA A.K., YADAV A.K., Sen. Trans. J., 92 (2008), 99.
[4] RAGHUPATHI P.S., GEORGE J., MENON C.S., Ind. J. Pure Appl. Phys., 43 (2005), 620.
[5] RAHMAN M.-U., YU G., KRISHNA K.M., SOGA T., JIMBO J.W.T., UMENO M., Appl. Opt., 37 (1998), 691.
[6] TANG H., PRASAD K., SANJINES R., SCHMID P.E., LEVY F., J. Appl. Phys., 75 (1994), 2042.
[7] NITTA T., TERADA Z., HAYABAWA S., J. Am. Ceram. Soc., 63 (1980), 295.
[8] MOON J., TSKAJI H., FUJISHIRO Y., AWANO M., J. Mater. Sci., 36 (2001), 949.
[9] CAROTTA M.C., FERRONI M., GNANI D., GUIDI V., MERLI M., MARTINELLI G., CASALE M.C., NOTARO M., Sens. Act. B, 58 (1999), 310.
[10] AKHTAR M.K., PRATSINIS S.E., MASTRANGELO S.V.R., J. Am. Ceram. Soc., 75 (1992), 3408.
[11] VEMURY S., PRATSINIS S.E., J. Am. Ceram. Soc., 78 (1995), 2984.
[12] BONINI N., CAROTTA M.C., CHIONINO A., GUIDI V., MALAGU C., MARTINELLI G., PAGLIALONGA L., SACERDOTI M., Sens. Act. B, 68 (2000), 274.
[13] ZHU B.L., XIE C.S., WANG W.Y., HUANG K.J., HU J.H., Mater. Lett., 58 (2004), 624.
[14] KALAYAMA K., HASEGAWA K., TAKAHASHI T., AKIBA T., YANAGIDA H., Sens. Act. A, 24 (1990), 55.
[15] KIM T.Y., LEE D.H., SHIM Y.C., BU J.U., KIM S.T., Sens. Act. B, 9 (1992), 221.
[16] MAKITA K., NOGAMI M., ABE Y., J. Ceram. Society Japan, 105 (1997), 595.
[17] YANG S.L., WU J.M., J. Mat. Sci., 26 (1991), 631.
[18] YOSHIMURA N., SATO S., ITOI M., TAGUCHI H., Sozai Busseigaku Zasshi, 3 (1990), 47.
[19] KULWICKI B.M., J. Amer. Ceram. Soc., 74.(1991), 697.
[20] MORIMOTO T., NAGAOAND M., TOKUDA F., J. Phys. Chem., 73 (1969), 243.

Received 7 June 2009
Revised 4 October 2009